3DXRD AT THE ADVANCED PHOTON SOURCE: ORIENTATION MAPPING AND DEFORMATION STUDIES

U. Lienert[1], M.C. Brandes[2], J.V. Bernier[3], M.J. Mills[2], M.P. Miller[4], S.F. Li[5], C.M. Hefferan[5], J. Lind[5], R.M. Suter[5]

[1]Argonne National Laboratory,
9700 S. Cass Ave., Lemont, IL 60439, USA
[2]Ohio State University, 477 Watts Hall, Columbus, OH 43210, USA
[3]Lawrence Livermore National Laboratory,
Livermore, CA 94551, USA
[4]Cornell University, 194 Rhodes Hall, Ithaca, NY 14853, USA
[5]Carnegie Mellon University, Department of Physics,
Pittsburgh, PA 15213, USA

ABSTRACT

The high-energy diffraction microscopy program at the 1-ID beamline of the Advanced Photon Source is based on the 3DXRD diffraction technique. Essential developments include a near field forward modeling algorithm, far field high-resolution reciprocal space mapping, continuous tensile deformation capability, and combination with *post mortem* electron microscopy. The beamline instrumentation is outlined and the status of the near and far field techniques is illustrated by selected case studies. The potential of the near field mapping technique to investigate orientation gradients in deformed metals is discussed and recent experimental results are presented on Ni and Al. The plastic deformation of a Ti-7Al alloy is investigated by a combination of far field diffraction and electron microscopy. Two material states of distinct dislocation microstructures are studied during continuous tensile deformation up to about 2% applied strain. Stress tensors of individual grains are evaluated and discussed in view to yield surface topology. The dislocation structures are investigated by high-resolution reciprocal space mapping and electron microscopy.

1. INTRODUCTION

The high-energy diffraction microscopy (HEDM) program at the 1-ID beamline, located at the Argonne National Laboratory (Argonne, IL), aims at the structural characterization of polycrystalline bulk materials during thermo mechanical processing. It is based on the 3DXRD diffraction principles, i.e. bulk penetrating high-energy synchrotron radiation, orientation contrast, and “tomographic” data acquisition using area detectors (Poulsen (2004)). Other essential components of the HEDM program include the development of thermo mechanical sample environment, data evaluation and reconstruction software, and the combination with complementary techniques such as electron microscopy or tomography. This paper outlines the present status and anticipated development of the HEDM instruments at the 1-ID beamline, and illustrates recent developments by selected case studies.

The diffraction geometry may be subdivided into the limiting near and far field cases. In the near field limit, the detector is close to the sample so that grain outlines are projected onto the detector. In case of grains of sufficient crystalline perfection, a 2D beam can be employed

Report Documentation Page

Form Approved
OMB No. 0704-0188

1. REPORT DATE	2. REPORT TYPE	3. DATES COVERED
2010		**00-00-2010 to 00-00-2010**

4. TITLE AND SUBTITLE	5a. CONTRACT NUMBER
3DXRD at the Advanced Photon Source: Orientation Mapping and Deformation Studies	5b. GRANT NUMBER
	5c. PROGRAM ELEMENT NUMBER
6. AUTHOR(S)	5d. PROJECT NUMBER
	5e. TASK NUMBER
	5f. WORK UNIT NUMBER
7. PERFORMING ORGANIZATION NAME(S) AND ADDRESS(ES) **Carnegie MellonUniversity ,School of Computer Science,Pittsburgh,PA,15213**	8. PERFORMING ORGANIZATION REPORT NUMBER
9. SPONSORING/MONITORING AGENCY NAME(S) AND ADDRESS(ES)	10. SPONSOR/MONITOR'S ACRONYM(S)
	11. SPONSOR/MONITOR'S REPORT NUMBER(S)

12. DISTRIBUTION/AVAILABILITY STATEMENT
Approved for public release; distribution unlimited

13. SUPPLEMENTARY NOTES
Risoe 2010 Symposium proceedings, Challenges in materials science and possibilities in 3D and 4D characterization techniques, p. 59, N. Hansen, D. Juul Jensen, S.F. Nielsen, H.F. Poulsen, and B. Ralph, editors (2010). U.S. Government or Federal Rights License

14. ABSTRACT
The high-energy diffraction microscopy program at the 1-ID beamline of the Advanced Photon Source is based on the 3DXRD diffraction technique. Essential developments include a near field forward modeling algorithm, far field high-resolution reciprocal space mapping continuous tensile deformation capability, and combination with post mortem electron microscopy. The beamline instrumentation is outlined and the status of the near and far field techniques is illustrated by selected case studies. The potential of the near field mapping technique to investigate orientation gradients in deformed metals is discussed and recent experimental results are presented on Ni and Al. The plastic deformation of a Ti-7Al alloy is investigated by a combination of far field diffraction and electron microscopy. Two material states of distinct dislocation microstructures are studied during continuous tensile deformation up to about 2% applied strain. Stress tensors of individual grains are evaluated and discussed in view to yield surface topology. The dislocation structures are investigated by high-resolution reciprocal space mapping and electron microscopy.

15. SUBJECT TERMS

16. SECURITY CLASSIFICATION OF:			17. LIMITATION OF ABSTRACT	18. NUMBER OF PAGES	19a. NAME OF RESPONSIBLE PERSON
a. REPORT **unclassified**	b. ABSTRACT **unclassified**	c. THIS PAGE **unclassified**	**Same as Report (SAR)**	**20**	

illuminating a sample volume. However, with increasing mosaicity spot overlap becomes prohibitive, and eventually a 1D line beam must be used that illuminates only a sample layer. A forward modeling approach is described for this geometry and grain orientation maps are presented. The applicability of the approach to plastically deformed materials and the mapping of orientation gradients are discussed.

In the far field limit, the detector distance is much larger than the sample dimensions. This provides ample space for sample environment. The strain sensitivity is dramatically improved but only the center-of-mass grain positions are measured (aspect ratios may be obtained by the "box scan methodology"). At intermediate detector distances, several complete diffraction rings are recorded, as on the near field detector, and the azimuthal width of a detector pixel is about 0.1 deg. By moving the detector even further back and using a narrow bandwidth x-ray beam, the reciprocal space resolution is increased such that peak broadening due to dislocation structures can be quantified. Both medium and high-resolution reciprocal space far field diffraction are demonstrated by an investigation of the plastic deformation of a Ti-7Al alloy on the grain and subgrain length scales. Electron microscopy (EM) was performed post mortem on the same samples and subsets of grains after in situ far field measurements during uninterrupted tensile deformation. EM is a local probe providing spatial resolution from the micrometer to the atomistic length scales. Serial sectioning is applied to obtain bulk information. A variety of EM techniques are applied that map the crystallographic orientation and lattice strains, and determine dislocation characters, distributions, and densities.

2. BEAMLINE OPTICS, INSTRUMENTATION, AND RECIPROCAL SPACE RESOLUTION

2.1 Optics and instrumentation. The first element of the 1-ID x-ray optics is a double bent Laue monochromator with vertical diffraction plane and cryogenically cooled first crystal (Shastri (2004)). This monochromator provides a relative energy bandwidth of about 10^{-3}, which is well matched to the resolution of area detectors that cover complete diffraction rings. The bandwidth is also compatible with strain measurements to an uncertainty of 10^{-4} or better by determining the centers of diffraction peaks. However, better resolution is desirable for the interpretation of the actual peak shapes in terms of dislocation structure.

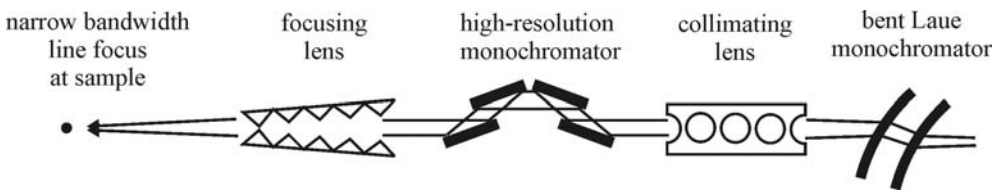

Fig. 1. X-ray optics employed for the high-resolution reciprocal space mapping (Shastri et al. (2007)).

For the near field mapping, a horizontal line focus is obtained by Si saw tooth compound refractive lenses (CRLs). The near field mapping setup is located in the 1-ID-B hutch. Essential components are a high precision air bearing stage and a high-resolution imaging detector. The far field experiments are performed in the 1-ID-C hutch. For the high-resolution reciprocal space mapping, the x-ray beam is collimated by compound refractive lenses and then the bandwidth is reduced to 7×10^{-5} by a four bounce flat Si 111 monochromator. The beam is then focused vertically by CRLs (see Fig. 1). A 5 kN screw driven uniaxial load frame has been designed that is mounted on a xyz-stage to the ϕ rotation table of a four circle diffractometer (see Fig. 2). The load frame can be rotated by ±180 deg around the ϕ and χ rotation axes (except for ±10 deg direct beam obstruction around the ϕ axis) and therefore provides large pole figure coverage. For medium resolution far field diffraction usually an amorphous Si detector (GE 41RT) is employed (detector A) (Lee et al. (2008)). This detector can buffer up to 300 frames in memory with a frame rate of up to eight frames per second and can be synchronized to continuously turning rotation axes. For the high-resolution reciprocal space mapping usually a fiber optics tapered CCD (MAR165) is mounted on a vertical translation stage about 3.8 m downstream of the sample (detector B).

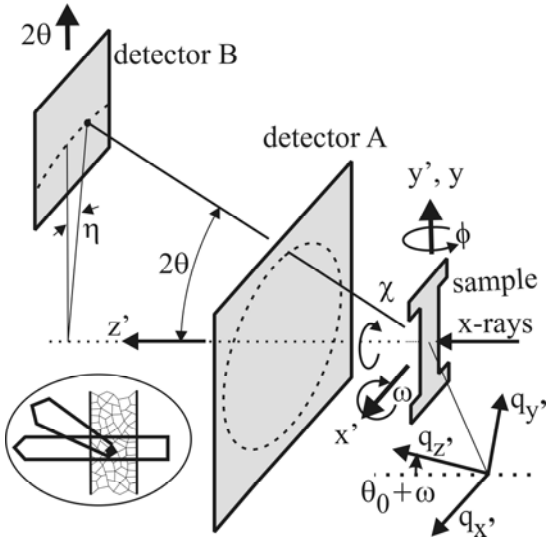

Fig. 2. Far field diffraction setup in the 1-ID-C hutch (from Lienert et al. (2009)).

2.2 Reciprocal space resolution. The high-resolution reciprocal space mapping setup is shown in Fig. 2 and described by Jakobsen et al. (2007). The $q_{x'}$, $q_{y'}$, $q_{z'}$ reciprocal space coordinate system is chosen such that $q_{y'}$ is parallel to the reciprocal lattice vector, $q_{x'}$ is parallel to the laboratory x' direction, and $q_{z'}$ is perpendicular to $q_{x'}$ and $q_{y'}$. $q_{x'}$ and $q_{z'}$ therefore span the azimuthal plane but the respective reciprocal space directions depend on the grain orientation. In general, the reciprocal space intensity distribution of deformed metals displays distinct distributions parallel and perpendicular to the reciprocal lattice vector. The radial projection is usually dominated by coherent strain broadening (with the strain component in $q_{y'}$ direction given by $-q_{y'}/|q_0|$) whereas the azimuthal distribution of deformed grains is dominated by the incoherent superposition of misoriented domains (with misorientations given by $q_{x',z'}/|q_0|$). For small $q_{x'}$ and $q_{z'}$ (i.e. small misorientations) the first order transformation from the experimental quantities θ, η, ω to reciprocal space is given by

$$q = \begin{pmatrix} q_{x'} \\ q_{y'} \\ q_{z'} \end{pmatrix} \approx |q_0| \begin{pmatrix} -\eta \cos(\theta_0) \\ \dfrac{(\theta - \theta_0)}{\tan(\theta_0)} \\ \omega - (\theta - \theta_0) \end{pmatrix}. \qquad (1)$$

This approximation holds for coherently diffracting domains such as subgrains (Jacobsen et al. (2006)) or the below discussed LaB_6 domains. For deformed grains with an orientation spread of several degrees, higher order terms are required but the separation of radial and azimuthal distributions is still of descriptive value.

The instrumental resolution of the high resolution reciprocal space mapping was quantified by mapping 421 reflections of individually scattering LaB_6 domains, the length of the reciprocal lattice vector being $|q_0| = 2\pi/d_{hkl} = 6.93 Å^{-1}$. The domain size was estimated from x-ray line profile analysis and TEM to be about L = 2μm (NIST (2000)) which gives a size broadening of $\Delta q_{size} = 2\pi\ k/L = 0.26 \cdot 10^{-3} Å^{-1}$ (with a Scherrer constant k = 0.829). In units of angular spread in the azimuthal plane, Δq_{size} equals $2.1 \cdot 10^{-3}$deg and, expressed as strain in radial direction, is $38 \cdot 10^{-6}$.

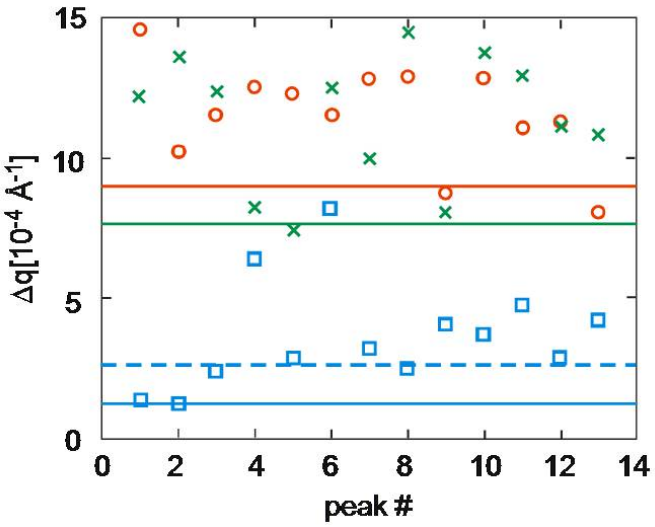

Fig. 3. Widths of diffraction peaks from individual LaB_6 powder domains (FWHM) in $q_{x'}$ (crosses), $q_{y'}$ (circles), and $q_{z'}$ (squares). Solid lines indicate the instrumental resolution calculated from the beam divergences, detector resolution, and ω rocking interval. The dashed blue line indicates the size broadening q_{size}.

Details are given in Jakobsen (2006b). We note that the narrowest peak widths are in good agreement with the estimated resolution from instrumental parameters. Due to the small scattering angles, the $q_{z'}$ resolution is significantly better than $q_{x'}$ and $q_{y'}$ since the beam divergences and detector resolution mainly effect the latter.

3. NEAR FIELD FORWARD MODELLING

3.1 Reconstruction of microstructure. Our basic approach has been described in detail (Suter, et al. 2006). The experimental geometry and coordinate system are shown schematically in Fig. 4. The line focused high-energy x-ray beam illuminates a planar section of the sample and diffraction patterns are imaged on an area detector positioned behind the sample. Each image is collected as the sample is rotated through a small integration interval, $\delta\omega$, and such intervals are measured over a range of 180 degrees. This sequence is repeated at two or three sample-to-detector distances, L. This means that many (~50) Bragg peaks are collected from arbitrary crystal orientations yielding many projections that are imaged on the high spatial resolution near field detector. In performing reconstructions of the orientation field, we do a computer simulation of the experiment and sample microstructure by gridding the illuminated sample plane with equilateral triangles (voxels) and simulating diffraction for a set of candidate crystal orientations. The algorithm searches for orientations that generate scattering that matches that seen in the experimental data set. Each voxel is adjusted independently of all others. Typically, we use a mesh with voxels with side lengths comparable to the effective detector pixel size. While this procedure is computationally costly, the aim is to extract as much information from the data set as possible. As illustrated below, we obtain not only the shapes of "grains" but also considerable information about grain boundary shapes and character and orientation disorder within grains.

3.2 Orientation resolution. We recently showed that the spatial resolution of reconstructions is, under ideal conditions, limited by the detector spatial resolution (Hefferan et al. (2009)). We found from fits to a simulated microstructure with two micron features (boundary position roughness) that errors are reduced by more than a factor of 10 when comparing a data set with 4 micron detector pixels to one with 1.5 micron pixels. In these simulations using perfectly ordered grains, we also found orientation noise at the level of 0.1 degree inside of grains. A similar noise level was found in reconstructions of experimental data measuring fully-recrystallized grains in a nickel sample as well as in orientation statistics in the same sample (Hefferan et al. (2010)). This low orientation uncertainty or error bar might be surprising at first since we do measurements while the sample rotates through an interval of $\delta\omega = 1$ degree. However, this can be understood just from the fact that many Bragg peaks are observed in specific ω intervals over the 180 oscillation intervals.

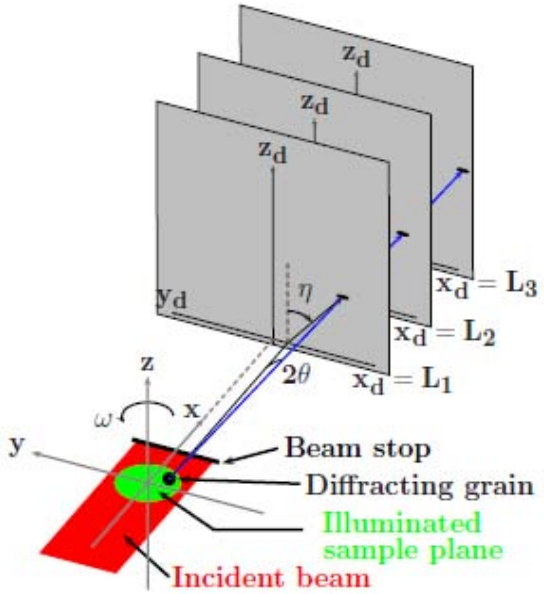

Fig. 4. Schematic of the mapping measurement as described in (Poulsen (2004), Suter et al. (2006)).

A reciprocal lattice vector, G_{hkl}, is brought into the Bragg condition through the rotation ω about the normal to the beam plane. If the projection of G_{hkl} into the xy-plane at ω = 0 is $G_{hkl\perp} = |G_{hkl}| \sin\chi\ (\cos\phi\ \hat{i}\ + \sin\phi\ \hat{j}\ )$, with χ being the tilt of G_{hkl} away from the z-axis, then the Bragg condition can be written, using Fig. 4, as

$$2\mathbf{k}_i \cdot \mathbf{G}_{hkl} = 2k\left|\mathbf{G}_{hkl}\right| \sin\chi \cos(\phi+\omega) = -\left|\mathbf{G}_{hkl}\right|^2 \qquad (2)$$

or, using $|\mathbf{G}_{hkl}| = 2k \sin\theta$, with θ being the Bragg angle, we have

$$\cos(\phi+\omega) = \frac{-\sin\theta}{\sin\chi}. \qquad (3)$$

This clearly requires the well known condition that $\chi \geq \theta$ with $0 < \theta \leq \pi/2$. χ and ϕ are unique specifiers of the (hkl) plane orientation at ω = 0, that is, in a sample reference frame. The forward model searches over a fundamental zone of physically distinct orientations for one that generates a match of N observed (χ,ϕ) pairs. The three crystal orientation parameters determine the entire set of pairs. Since N ≈ 50, the problem is highly overdetermined. Merely fitting the Bragg positions of indexed peaks into the correct ω intervals is highly constraining. If we take the true Bragg ω positions as falling quasi-randomly within each δω interval, then one tenth of the peaks will occur within 0.1 degree of the edge of the interval.

If N = 50, then five peaks occur within this limit meaning that changing the orientation by ~0.1 degree can move that peak to a different measurement interval. The same scenario applies at each end of the interval. Thus, measuring a large set of Bragg values of ω is likely to be sufficient to yield the observed 0.1 degree sensitivity. We expect that scaling down

the integration interval, δω, will yield reduced orientation uncertainty. A continuous rotation and readout scheme could yield a resolution on the order of that intrinsic to the x-ray setup.

3.3 Mapping of strained samples. With 0.1 degree or better orientation resolution and spatial resolution approaching a micron, it is reasonable to investigate the possibility of mapping orientation fields in deformed materials. As a test, we have carried out a simulated experiment. We start with a three dimensional orientation field provided by Dawson's group at Cornell University that was computed as the result of straining a simulated polycrystal composed of hexagonal crystal symmetry grains. We extracted orientations from a single two-dimensional cut through the center of the simulated volume. This orientation field, shown in Fig. 5a, was used to generate a set of binary detector images using experimental parameters similar to those we use at the APS 1-ID beamline. The simulated detector has 1024 by 1024 pixels with four micron pitch (more recent work at the APS uses a detector with 2048 by 2048 pixels with 1.5 micron pitch; a simulation with this configuration would presumably improve on the results shown here). Two example detector images are shown in Fig. 6; these images correspond to one degree ω integration intervals separated by five degrees in ω. Numerous arcs of intensity can be seen. These correspond to smearing of scattering from individual grains due to the orientation gradients visible in Fig. 5a. The visibility of individual points in the arcs (rather than continuous streaks) is due to the discreteness of the simulated structure. The colored arcs (identical in the two images) are drawn as guides to the eye: they are drawn so as to intersect scattering in (a) and to make it apparent that different arcs have different origins. While the blue and red arcs have the same origin, the green one is shifted by 112 microns indicating scattering originating from a different part of the structure. The detector images also show, as expected, that the scattering is spread not only in η as shown on individual images but also in ω since numerous arcs are repeated in the two images. The details of the patterns evolve slowly with ω. For example, the intensity on the right end of the blue arc in (a) is not in (b).

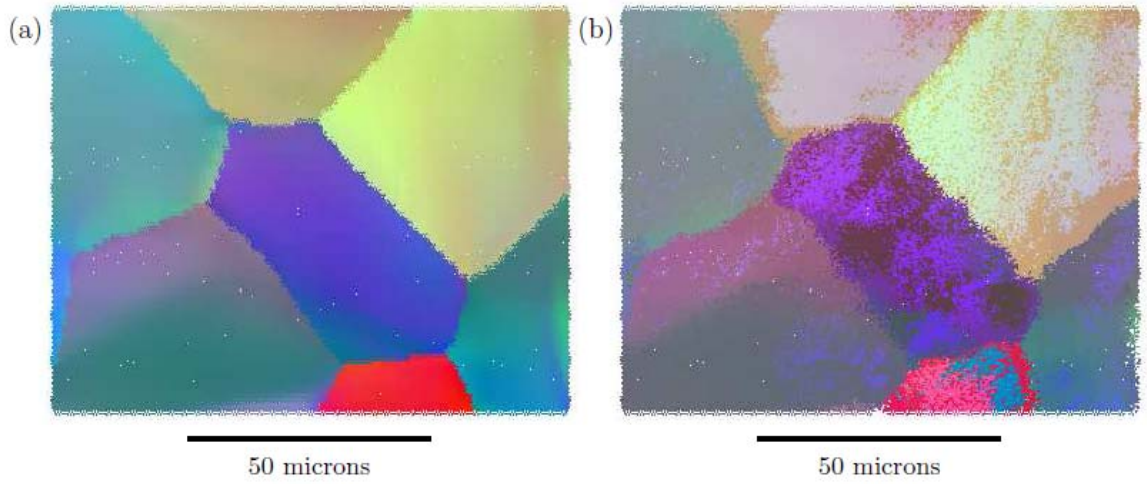

Fig. 5. (a) Orientations extracted from a simulation of 20% deformation of a hexagonal polycrystal. (b) The reconstructed structure obtained from the simulated scattering data from the structure in (a). RGB color contributions are mapped from the Rodrigues vector components required to rotate the crystal lattice from a laboratory reference frame to their orientation in the simulated structures.

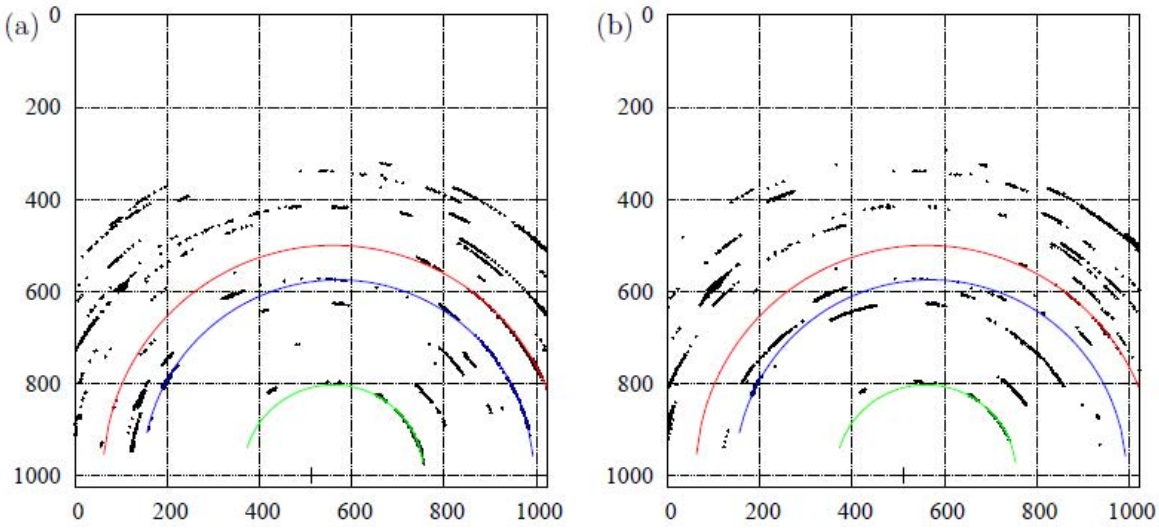

Fig. 6. Example detector images generated from the orientation field in Fig. 5a and used as the input data set for the reconstruction in Fig. 5b. The patterns are separated in ω by five degrees. Axes are labeled with pixel numbers where the pixels are $4 \times 4\mu m^2$. The '+' at the bottom labels the detector origin which is the intersection of the projections of the rotation axis and incident beam onto the detector. The colored lines are guides to the eye that pass through arcs of scattering. See the text for details.

We ran our reconstruction code using the simulated detector images as input data. The fit began with an empty orientation field. Fig. 5b shows the result. While not a perfect reproduction of (a), the reconstruction shows similar grain structure to that of the input. The positions of triple points are reproduced quite well. Furthermore, substantial information about intra-granular orientation gradients is reproduced. While we continue to perform more detailed tests, this result implies that near field studies of strained materials should yield substantial information about orientation gradients and their development under different processing conditions. The combination of such maps with the far field measurements described in detail below, should yield detailed multi-parameter data sets that can be used to constrain computational models of plasticity.

3.4 Case studies. Fig. 7 shows reconstructions of single layers of two samples: (a) a fully recrystallized high purity nickel sample (one of 42 layers collected and reconstructed) and (b) an as received high purity aluminium wire (one of 11 layers). These images contain roughly 98,000 equilateral triangle mesh elements (voxels) with edge lengths of 5.7 and 4.7 microns, respectively. The orientation in each voxel has been optimized independently from others. Colors are obtained by weighting red, green, and blue contributions proportional to Rodrigues vector components specifying the local crystallographic orientation. White regions inside the hexagonal reconstruction boxes were found to not have any orientation that generates scattering that matches the experimental data – in most cases, these white regions are simply outside of the sample. While the concept of a "grain" is not used by the reconstruction algorithm, it is clear that regions of uniform color correspond to somewhat uniform orientation and, thus, to grains. In addition to the orientation colors, we have drawn in Fig. 7 black lines along the edges of voxels whenever the orientation in neighboring voxels are different by more than a threshold value: 0.1 degree in (a) and 0.5 degree in (b). These lines decorate grain boundaries but also show

misorientations within grains. In the nickel, most grains have no internal orientation discontinuities at the 0.1 degree level whereas the aluminium grains have many discontinuities even at the 0.5 degree level. The level of precision in (a) is consistent with our tests using simulated structures (Hefferan et al. (2010)). Thus, the few intragranular features (black lines) may be a combination of noise and real gradients. Some of the intragranular disorder in (b) should be interpreted as statistical and only slightly above the noise level in this early data set. However, numerous organized features (continuous sets of >0.5 degree discontinuities) appear in adjacent layer data sets as well as in data sets collected from this same layer after annealing. These low angle structures and their annealing behaviour will be described in a forthcoming publication.

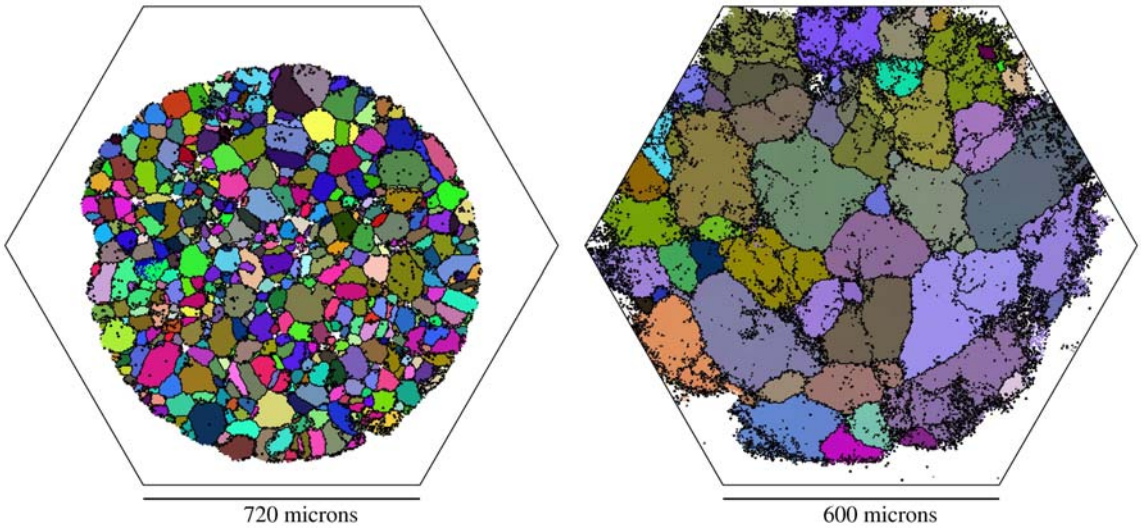

Fig. 7. (a) Reconstructed layer of fully recrystallized Ni and (b) of as received high purity aluminum. The average grain sizes (circle equivalent diameter), based on a threshold of two degrees, are ~40 microns in (a) and ~80 microns in (b). See text for details.

4. TI-7AL SAMPLES AND DEFORMATION PROCEDURE

Details of the sample preparation are given in Lienert et al. (2009). The extruded material was further processed to produce an equiaxed grain structure with an average line intercept grain size of ~75 µm. Two material states were prepared by altering the cooling procedures. Short range order (SRO) domains precipitated during slow air-cooling (AC), but are not present after ice water quenching (IWQ). The presence of SRO domains is known to lead to planar slip bands during tensile deformation, whereas a spatially homogeneous dislocation structure is observed in the quenched material state. Flat, hourglass-shaped specimens of 1 mm thickness and a gage section of 2.5 mm × 12 mm were cut by electrical discharge machining from both the AC and IWQ materials such that the deformation axis was parallel to the extrusion direction of the bar.

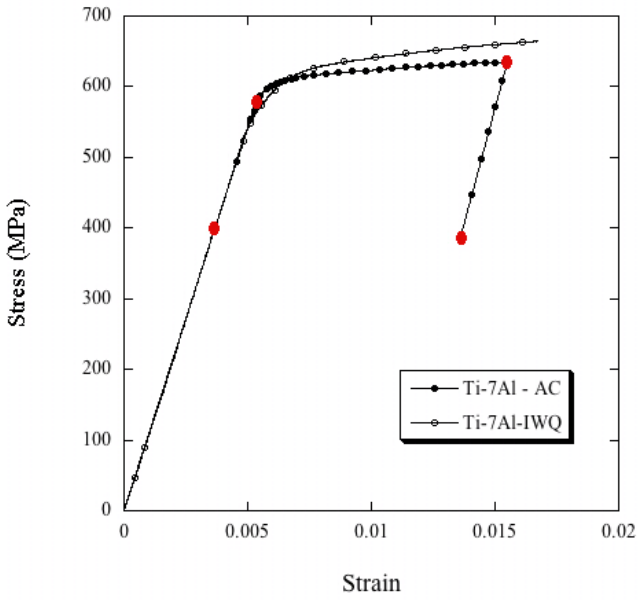

Fig. 8. Loading curves of the air-cooled (AC) and ice water quenched (IWQ) Ti-7Al samples. In our latest experiment, the samples were deformed continuously while x-ray diffraction patterns were acquired. Previously, we halted the loading to acquire diffraction data. The approximate macroscopic stress levels where the diffraction experiments described in Section 6 were conducted are depicted as the four red symbols.

Two synchrotron experiments were performed on both material types while samples were deformed up to about 2% in tension. Therefore samples were mounted in a screw driven tensile load frame which in turn was mounted on a xyz stage to a three circle goniometer providing rotations $\{\phi,\chi,\omega\}$ (Fig. 2). The first experiments were conducted in the interrupted in-situ manner: load the specimen to a specific macroscopic level then halt loading while diffraction patterns are acquired at various specimen orientations. The more recent experiments are completely different. Loading of the sample is not halted. Rather, the specimen was reoriented continuously and diffraction experiments were conducted as quickly as the detector could be reset. The advantage of the continuous loading experiment, and the motivation for its development, is the ability to capture lattice strains without interruption of the loading rate – without changing the deformation trajectory. The continuous loading data are currently being digested and will appear in a later publication. We focus here on the lattice strain measurements taken in the interrupted manner.

During these experiments, the load frame cross head is moved manually until a prescribed macroscopic stress level is reached. At this point, the load is reduced by 10% to avoid any viscous deformation effects. While holding the position constant at this point, the specimen was rotated continuously in ϕ – while acquiring diffraction data using detector A (see Fig 2). A more extensive description of these in situ loading experiments on the Ti-7Al is given in Lienert et al.

(2009). Fig. 8 shows macroscopic stress-strain curves for both AC and IWQ specimens during continuous loading.

5. ELECTRON MICROSCOPY

With regard to the interrogation of the internal structures of materials, electron microscopy techniques naturally complement the HEDM techniques developed at the APS 1-ID-C beamline. EM techniques are particularly attractive for the examination of phase transformations and plastic deformation mechanisms where high spatial resolution is necessary for detailed structural analyses. Currently, users of the beamline are employing both scanning and transmission electron microscopy to augment their HEDM measurements. One example is presented in Fig. 9. At the SEM level, a number of techniques are employed for the post-mortem characterization of grain ensembles examined by the methods outlined here. Electron backscattered diffraction (EBSD) methods permit mapping of both crystal orientation and lattice strains. While conventional EBSD allows for the visualization of local crystal rotations and disorientations, more specialized techniques may be employed for the quantification of local strain states in deformed materials (Wilkinson et al. (2006)). Scanning imaging methods, like channeling contrast imaging, allow for the quantitative analyses of dislocation activity and the characterization of active slip systems (Crimp et al. (2001)). Additionally, the information gathered at the SEM level may be extended to three-dimensional volumes with well-established serial sectioning and reconstruction algorithms (Singh and Gokhale (2005)). At the TEM level, microstructure is characterized in fine detail not captured by either HEDM or SEM based analyses - with the aid of focused ion beam milling, these experiments are conducted at specific regions within the x-rayed volume. Diffraction contrast techniques allow for the determination of dislocation characters, distributions, and densities, and convergent beam diffraction experiments permit the quantitative measurement of crystallographic misorientations due to substructure formation. These techniques, in concert with advanced TEM experiments, i.e. lattice imaging, energy filtered imaging, and spectroscopy, provide for the examination and analyses of material chemistry and secondary phases that influence deformation behavior at length scales as small as ~0.05 nm.

The master grains of the Ti-7Al samples investigated by HEDM have been located, and EM techniques are providing for measurements of spatially resolved strain distributions, dislocation densities, and slip system activities in grains of interest as well as the surrounding regions.

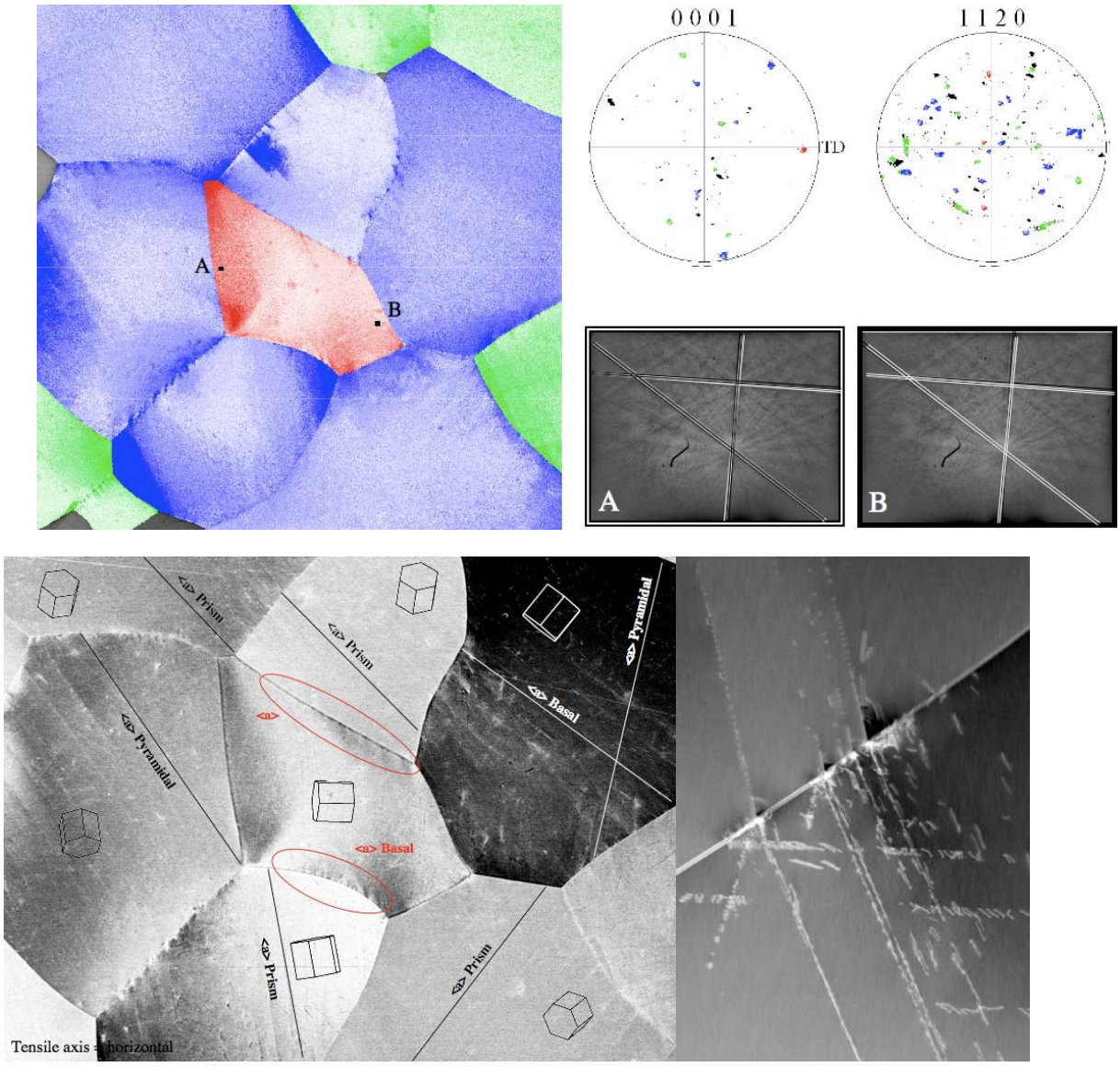

Fig. 9. EM observations of an internally situated ensemble of grains that were first examined through HEDM experiments. **Top left**: A conventional EBSD map with color gradations (white to color = 2 deg) according to the pole figures presented at top right. **Middle right**: High-resolution EBSD patterns taken at points A and B in the EBSD map; overlays of selected bands (white lines) from pattern A in pattern B (black lines) demonstrate the strain and rotational sensitivity of the technique. **Bottom left**: SEM electron channeling contrast image demonstrating the capability to determine slip activity and character in deformed grains at the SEM level. Contrast variation within grains gives indication of local lattice curvatures due to long range stress fields and dislocation content. **Bottom right**: Dark field scanning transmission electron image of dislocation pile-ups at a grain boundary. Note that the variation in background contrast across slip bands is a result of local crystal misorientations that may be quantified by convergent beam electron diffraction techniques.

6. FAR FIELD DIFFRACTION AT MEDIUM AND HIGH MOMENTUM RESOLUTION

6.1 Grain resolved lattice strains and crystal stresses by medium resolution far field diffraction.
A detailed description of the lattice strain experiments can be found in (Lienert et al. (2009)). We present an outline here. This experiment employed detector A (Fig. 2), which, at a distance of about 883 mm behind the sample, enabled collection of several complete diffraction rings. The x-ray energy was 52 keV and the beam size 300 μm × 150 μm (horizontal × vertical). At each target load, diffraction images were acquired while rotating the sample over $\phi \in \{-60°, 60°\}$ in continuous 1° steps at a typical acquisition time of 1 second per frame. A preliminary scan of the unloaded specimen was conducted and 18 grains were chosen near the specimen axis – away from the specimen surface. From this list, one of which was selected as the "master grain". Throughout the experiment, the beam and rotation axis were both centered on the master grain. The strain states of the 18 grains were evaluated from the lengths of the 15-20 measured scattering vectors, q, per grain. The lengths of the unstrained reciprocal lattice vectors were obtained as the azimuthal average of diffraction images of an unstrained sample summed over all ϕ angles. The evaluation procedure takes into account that grains are not centered on the rotation axis. The shifts of reflection are due to the distortions of the crystal lattice (lattice strains) and also due to the offsets of the grains relative to the rotation axis. Details of the strain evaluation may be found in Bernier et al. (2010). The lattice strain tensor being experienced by each grain at each of the target loads is determined using a least-squares routine. The grain specific stress tensors were calculated from the strain tensors using single-crystal elastic constants, obtained from a Ti-6Al alloy (Kim et al. (2002)). The stress tensors for four grains within the AC specimen (#1, #5, #10 and #11) at four macroscopic stress levels (shown in Fig. 8) are shown in Fig. 10.

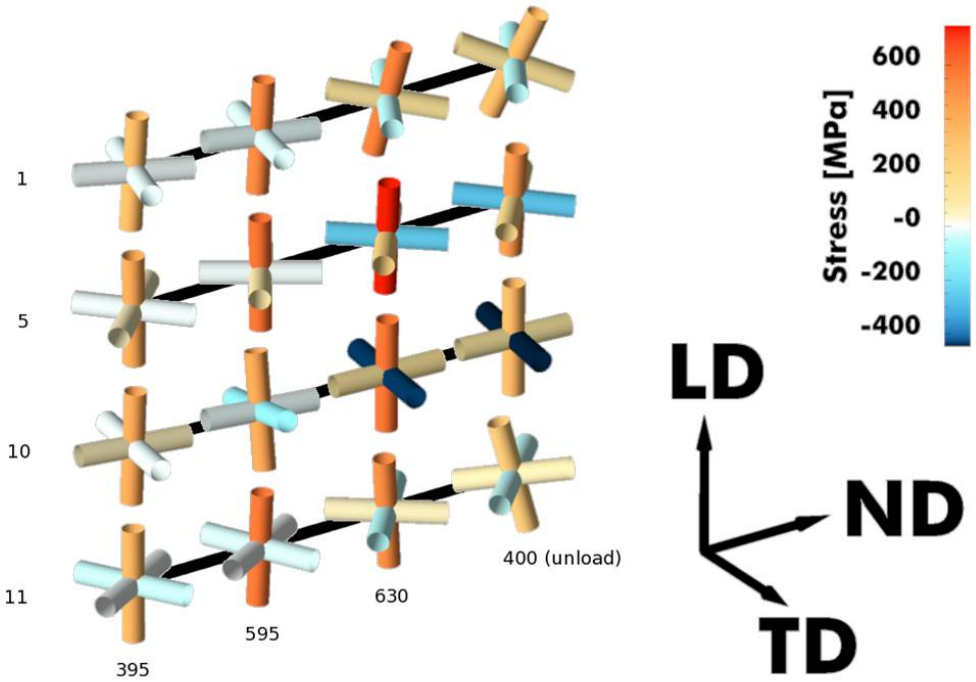

Fig. 10. Principal stress triads or "jacks" depicting the orientation and magnitude of the principal stresses experienced by four grains within the deforming AC specimen at the indicated macroscopic stress levels (in MPa). The relevant specimen directions, LD (loading direction), TD (transverse direction) and ND (normal directions) are also depicted as is a stress color bar.

During a uniaxial tension test, the macroscopic stress—jack would have one leg of the jack exactly aligned with the loading direction (LD) coloured according to the four nominal stress values. The other two legs would be the color associated with zero stress (light tan). As can be seen, each of the crystals at the nominal stress of 400 MPa begin with the maximum principal stress roughly aligned with LD. However, they have various values for the other two principal stresses – not necessarily zero nor aligned with ND and TD. The stress-jacks roughly scale (change color but not orientation) between 395 MPa and 595 Mpa, which is very near the macroscopic yield strength. Between 595 MPa and 630 MPa all crystals will have yielded. The reorientation and re-colouring of the stress—jack legs are consistent with the change in stress "direction" that occurs as the stress state associated with each crystal moves towards a "vertex" on the single crystal yield surface (Kocks (1970)). Note that the reorientation of the stress tensor does not necessarily involve any reorientation of the crystal. The rotation we are referring to is of the stress—jack. Simulations are currently being conducted to ascertain whether these rotations of the stress tensor are consistent with the single crystal vertices employed in polycrystal plasticity simulations. There are slight reorientations of the stress—jacks as the specimen is unloaded from 630 MPa back to 400 MPa. As with the elastic-plastic transition in each crystal, these stress state rotations are consistent with moving off of the yield surface – where the crystal stress state is attempting to stay near a vertex—back into the deformation regime where elasticity-dominates both magnitude and direction. The plasticity-induced residual stresses within each crystal are easily observed by comparing the stress—jacks during the loading excursion near 395 MPa to the stress—jacks at 400 MPa during the unload. The crystal stress states within the aggregate must still integrate to the uniaxial value 400 MPa and the other components zero. However, these results demonstrate how differently the crystal stresses are distributed within the sample after a plastic excursion of less than 2% (see Figure 8). This understanding will greatly enhance our ability to predict crystals that may end up "at risk" during elastic-plastic processes such as fatigue. More importantly, these data can be invaluable when used in conjunction with crystal—based simulations to create a complete picture of the effects of deformation processes on the grain and subgrain scale.

6.2 Intragranular dislocation structure by high-resolution reciprocal space mapping. Here we describe high-resolution reciprocal space mappings of the selected master grains during the first experiment when loading was halted while diffraction data were acquired. The IWQ and AC master grains had different orientations with angles between their c-axes and the loading direction of 28.7° and 81.0°, respectively. Details of the experimental procedure are given in Lienert et al. (2009). For the high-resolution reciprocal space mapping, detector A is translated out of the beam, the selected reciprocal lattice vector is brought into the vertical scattering plane by an appropriate χ rotation, and detector B is moved to the appropriate height to capture the selected reflection (Fig. 2). Three-dimensional reciprocal space maps are then recorded by rocking the sample by narrow angle intervals around the ω-axis. In the following, reciprocal space intensity distributions at the highest sample deformations will be discussed. In Fig. 11 azimuthal (a) and radial (c) projections are shown for the IWQ master grain. The mosaicity of the undeformed grain is negligible compared to the orientation spread in the azimuthal

projection. The orientation spread is anisotropic with extreme directions closely aligned to high symmetry crystallographic directions. Fig. 11b is a map of the radial center-of-mass positions along the specific orientation fibers (i.e. orientation-weighted strain). An orientation dependent strain gradient is discernable which also shows when the radial projections along selected fibers are plotted (Fig. 11c). The profiles along the fibers at the extreme COM positions in Fig. 11b are shifted and the grain integrated profile is broadened compared to the profile along the fiber of the peak intensity.

The anisotropic azimuthal broadening is consistent with preferred slip system activity as evidenced by TEM observations. A significantly more anisotropic broadening is observed for the AC master grain, which is consistent with the planar slip band formation as revealed by TEM and larger grain rotations in the AC vs. IWQ samples. The AC master grain also displayed significantly stronger strain gradients, such that no peak shape analysis could be performed. However, peak shape analysis was performed for the IWQ master grain for the grain integrated and peak intensity fiber profiles (green and black peaks in Fig. 11c, respectively). The restricted random dislocation model by Wilkens ((1970a), (1970b)) was employed which describes peak broadening in terms of two fit parameters, dislocation density, and dislocation distribution parameter, M. M is sensitive to the shape of the radial profile, which may vary from Gaussian to Lorentzian depending on dislocation distribution. For reference, M >> 1 is associated with dislocation arrays with long-range stress fields and M ~ 1 describes homogenously distributed dislocations (Wilkens (1970a)). Based on the TEM results, the IWQ material shows a random distribution of screw dislocations of weak dipole character; this should be associated with an M factor slightly larger than 1. For fitting the model, dislocations having both a line orientation and Burgers vector of $\frac{a}{3}[\bar{1}2\bar{1}0]$ were assumed to be present in the grain. The fits to the radial profile of the azimuthal peak intensity fiber and to the grain integrated profile yielded dislocation densities of 0.9×10^{14} m^{-2} and 3.0×10^{14} m^{-2}, and M factors of 4.1 and 1.1, respectively (Fig. 12). The magnitude of the dislocation density determined from the radial profile of the specific orientation fiber at the azimuthal peak intensity position is in close agreement with a value of about 10^{14} m^{-2} estimated from literature data. For the literature value, alloying trends extrapolated from x-ray investigations in dilute (c_{Al} < 4 at%) binary Ti-Al alloys (Ghosh et al. (2001)) were applied to strain dependencies reported for TEM measurements on commercial purity grade alloys (Conrad (1981)). The differences between the two profiles indicate, however, that even for the IWQ case, intra-granular strain gradients have a significant impact on radial peak profile evaluation.

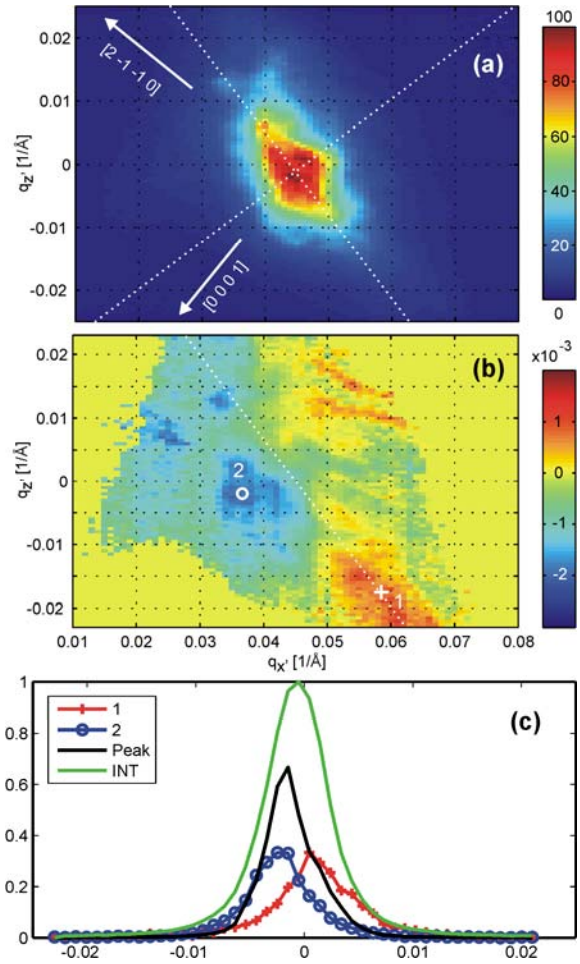

Fig. 11. Representations of the $(0\bar{2}20)$ IWQ mater grain reciprocal space map at 660 MPa. (a) Azimuthal intensity projection. The dashed lines indicate the directions of the narrowest and widest widths at half maximum. (b) Center-of-mass positions of radial profiles. (c) Selected radial profiles with arbitrary intensity scale for better visibility: azimuthal positions '1' and '2' are indicated in (b), at the azimuthal peak intensity (intersection of dashed lines in (a)), and azimuthally integrated (from Lienert et al. (2009)).

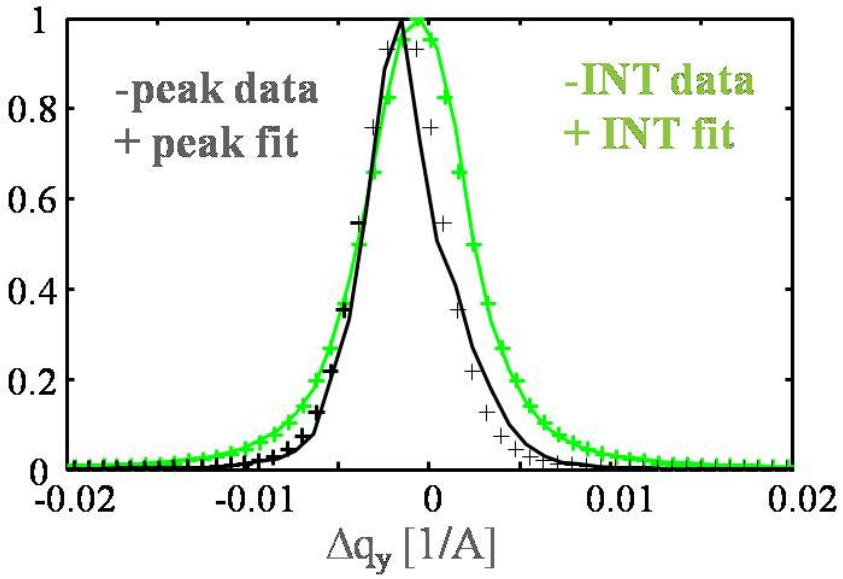

Fig. 12. Normalized radial profiles of the IWQ Ti-7Al reference grain after 2% tensile deformation. Plotted are the grain integrated profile (green line) and the profile along the fiber of maximum intensity in an azimuthal intensity projection (black line). The crosses indicate respective fits of Wilkens' restricted random dislocation distribution model.

5. SUMMARY

The 1-ID beamline at the Advanced Photon Source is a dedicated high-energy beamline equipped with x-ray optics that are optimized to provide micro-focused x-ray beams over an energy range of about 50-120 keV. The high-energy diffraction microscopy program has grown to a major user program. At present the near and far field setups are accommodated in separate hutches but an extension hutch is being designed that will be dedicated to HEDM and enable the combination of near and far field setups.

A near field forward modeling algorithm has been developed for an experimental line focus geometry. At present, the diffraction images are intensity thresholded and massively parallel computing is employed for the analysis. Orientation maps of several hundred grains per layer have been reconstructed for undeformed samples and simulated data of a 20% deformed Ti sample were reconstructed with good fidelity including intra-granular orientation gradients. The orientation uncertainty is estimated to be around 0.1 deg, limited by the present rotation step width of 1 deg. Resolution improvement by a factor of five to ten times seems feasible without increased acquisition time by continuous rotation data acquisition. Ongoing instrumental developments include a semi-transparent detector with one micrometer pixel size, simultaneous tomography, and thermo mechanical sample environment. Ongoing software developments include more efficient orientation search algorithms, and the fitting of diffraction intensity profiles. However, already the present capabilities provide significant micro-structural information within metallic bulk samples during annealing

The far field geometry provides ample space for sample environment, increased strain sensitivity but spatial information is mainly limited to center-of-mass positions of diffracting domains that display orientation contrast. Fast data acquisition up to about 5 deg/s is achieved

by continuous rotation scans using an amorphous silicon flat panel detector. In suitable cases, the strain tensors and center-of-mass positions of several hundred grains can be measured within a few minutes by the simultaneous refinement of strain and center-of-mass positions. Alternatively, grain positions (and aspect ratios), can be measured independently of the strain states within few hours by the "box scan" methodology. The orientation resolution as given by one pixel of the large area detector is about 0.1 deg. An order of magnitude finer orientation resolution and a radial resolution of about 10^{-4} is provided by the high-resolution reciprocal space mapping setup, on the cost of reciprocal space coverage.

The elastic-plastic deformation behavior of a Ti-7Al alloy is investigated by a combination of *in situ* far field HEDM and *post mortem* electron microscopy. Two distinct material states were prepared by different annealing treatments. Upon plastic deformation, each state is known to contain distinct dislocation structures and rate sensitive strain hardening. Stress states of 18 grains were followed during interrupted loading in an initial experiment. Significant rotations of the crystal stress states were observed upon the onset of plastic deformation. Each crystal was subjected to a distinct stress state, which could be quite different from the uniaxial stress state of the specimen. High-resolution reciprocal space maps of selected grains indicated significant intra-granular strain gradients, in particular for the material state with planar dislocation structure. Dislocation densities were estimated for the material state with random dislocation structure and found to be in good agreement with literature values based on TEM observations. In a recent experiment, far field diffraction images were recorded *during* continuous tensile deformation up to 2% applied strain. This experiment avoids the stress relaxation and creep that occurs during typical loading interruptions. These data will enable determination of the stress state of each crystal while it remains on the single crystal yield surface. Furthermore, 12 reflections of selected master grains were mapped with high reciprocal space resolution. These data sets enable the reconstruction of the single grain orientation distribution function and generalized pole figure inversions such as the strain orientation distribution function. The distribution functions should reflect the particular dislocation structures, which were also investigated by *post mortem* electron microscopy.

ACKNOWLEDGEMENTS

Use of the Advanced Photon Source was supported by the U. S. Department of Energy, Office of Science, Office of Basic Energy Sciences, under Contract No. DE-AC02-06CH11357. MCB and MJM acknowledge the support of the Federal Aviation Administration under Grant #O8-G-009. MPM gratefully acknowledges the Office of Naval Research, Julie Christodoulou, Grant Officer for support of this work as part of the D 3-D Program, contract number N00014-05-1-0505. MPM also thanks the X-ray Science Division of the Advanced Photon Source and the Materials Science and Engineering Department at The Ohio State University for sabbatical support during AY 2007. Partial support of the MRSEC at CMU under NSF grant number DMR-0520425 and of the NSF Metals and Nanostructures program under DMR-0805100 is acknowledged.

REFERENCES

Bernier, J.V., Barton, N.R., Brandes, M., Miller, M.P., Lienert, U., and Mills, M.J. (2010). A Capability for exploring crystal plasticity using High Energy Diffraction Microscopy. In

preparation.

Conrad, H. (1981). Effect of Interstitial Solutes on the Strength and Ductility of Titanium. Prog. Mater. Sci. 26, 123-404.

Crimp, M.A., Simkin, B.A., and Ng, B.C. (2001). Demonstration of the g· b u × 0 edge dislocation invisibility criterion for electron channeling contrast imaging. Philosophical Magazine Letters, 81, *12*, 833.

Ghosh, J., Chattopadhayay, S.K., Meikap, A.K., and Chatterjee, S.K. (2008) J. Microstructure characterization of titanium-base aluminium alloys by X-ray diffraction using Warren-Averbach and Rietveld method. J. Alloys Comp. 453, 131.

Hefferan, C.M., Li, S.F., Lind, J., and Suter, R.M. (2009). Tests of Microstructure Reconstruction by Forward Modeling of HEDM Data. Advances in X-ray Analysis 53, Proc. of the 2009 Denver X-ray Conference, to be published in Powder Diffraction.

Hefferan, C.M., Li, S.F., Lind, J., Lienert, U., Rollet, A.D., Wynblatt, P., and Suter, R.M. (2010). Statistics of High Purity Nickel Microstructure From High Energy X-ray Diffraction Microscopy. Computers, Materials and continua, to be published.

Jakobsen, B., Poulsen, H.F., Lienert, U., Almer, J., Shastri, S.D., Sørensen, H.O., Gundelach, C., and Pantleon, W. (2006). Formation and subdivision of deformation structures during plastic deformation. Science 312, 889-892.

Jakobsen, B. In-situ studies of bulk deformation structures: static properties under load and dynamics during deformation (2006b), Ph.D. thesis, Roskilde University, Roskilde, Denmark.

Jakobsen, B., Poulsen, H.F., Lienert, U., and Pantleon, W. (2007). Direct determination of elastic strains and dislocation densities in individual subgrains in deformation structures. Acta Mater. 55, 3421-3430.

Kim, J.Y., Yakovlev, V., and Rokhlin, S.I. (2002). Line-focus acoustic microscopy of Ti-6242 alpha/beta single colony: Detrmination of elastic constants. AIP Conf. Proc. 615B, 1118.

Kocks, U.F. Metall. Trans. 1 (1970) 1121.

Lee, J.H., Almer, J., Aydiner, C., Bernier, J., Chapman, K., Chupas, P., Haeffner, D., Kump, K., Lee, P.L., Lienert, U., Miceli, A., and Vera, G. (2008). Synchrotron applications of an amorphous silicon flat-panel detector. J. Synchrotron Rad. 15, 477-488.

Lienert, U., Brandes, M.C., Bernier, J.V., Weiss, J., Shastri, S.D., Mills, M.J., and Miller, M.P. (2009). In situ single-grain peak profile measurements on Ti-7Al during tensile deformation. Mater. Sci. Eng. A 524, 46-54.

NIST. Standard reference material 660a lanthanum hexaboride powder line position and line shape standard for powder diffraction. NIST Certificate, 2000.

Poulsen, H.F. (2004). Three-Dimensional X-ray Diffraction Microscopy, Springer Tracts in Modern Physics 205. Ed. G. Hohler, springer, Berlin.

Shastri, S.D. (2004). Combining flat crystals, bent crystals and compound refractive lenses for high-energy X-ray optics. J. Synchrotron Rad. 11, 150-156.

Shastri, S.D., Almer, J., Ribbing, C., and Cederstrom, B. (2007). High-energy X-ray optics with silicon saw-tooth refractive lenses. J. Synchrotron Rad. 14, 204-211.

Singh, H. and Gokhale, A.M., (2005) Visualization of three-dimensional microstructures, Materials Characterization, 54, 21 – 29.

Suter, R.M., Hennessy, D., Xiao, C., and Lienert, U. (2006). Forward Modeling Method for Microstructure Reconstruction Using X-ray Diffraction Microscopy: Single Crystal Verification. Rev. Sci. Instr. 77, 1-12.

Wilkens, M., (1970a), The Determination of Density and Distribution of Dislocations in Deformed Single Crystals from Broadened X-Ray Diffraction Profiles. Phys. Stat. Sol. (a) 2, 359.

Wilkens, M., (1970b). *In Fundamental Aspects of Dislocation Theory*, edts. J.A. Simmons, R. de Witt, R. Bullough, Vol. II, 1195. *Natl. Bur. Stand. (US) Spec. Publ.* No. 317. Washington,

DC, USA.

Wilkinson, A.J., Meaden, G., and Dingley, D. J. (2006). High resolution mapping of strains and rotations using electron backscatter diffraction. Materials Science and Technology, 22, *11*, 1271.